Frontiers in Heat and Mass Transfer

Tech Science Press

DOI: 10.32604/fhmt.2024.048474

ARTICLE

Numerical Study of Temperature-Dependent Viscosity and Thermal Conductivity of Micropolar Ag–MgO Hybrid Nanofluid over a Rotating Vertical Cone

Mekonnen S. Ayano[1,*], Thokozani N. Khumalo[1], Stephen T. Sikwila[2] and Stanford Shateyi[3]

[1]Department of Mathematics, University of Eswatini, Kwaluseni, M201, Eswatini

[2]Department of Mathematical Sciences, Sol Plaatje University, Kimberley, 8301, South Africa

[3]Department of Mathematical and Computational Sciences, University of Venda, Thohoyandou, 0950, South Africa

*Corresponding Author: Mekonnen S. Ayano. Email: mekk_aya@yahoo.com

Received: 08 December 2023 Accepted: 29 January 2024 Published: 30 August 2024

ABSTRACT

The present paper examines the temperature-dependent viscosity and thermal conductivity of a micropolar silver $(Ag)-$Magnesium oxide (MgO) hybrid nanofluid made of silver and magnesium oxide over a rotating vertical cone, with the influence of transverse magnetic field and thermal radiation. The physical flow problem has been modeled with coupled partial differential equations. We apply similarity transformations to the non-dimensionalized equations, and the resulting nonlinear differential equations are solved using overlapping grid multidomain spectral quasilinearization method. The flow behavior for the fluid is scrutinized under the impact of diverse physical constraints, which are illustrated graphically. The results of the skin friction coefficient and Nusselt number varying different flow parameters are presented in the form of a table. It is observed that the main flow of the hybrid nanofluid, nano particle fraction of silver and Magnesium/water, enhances compared to the mono-nano fluid MgO as the coupling number increases. The application of studies like this can be found in the atomization process of liquids such as centrifugal pumps, viscometers, rotors, fans.

KEYWORDS

Micropolar fluid; hybrid nanofluid; radiation magnetohydrodynamic; rotating cone; overlapping grid; spectral quasilinearization

1 Introduction

Thermal properties of most base fluids used in industry are low and do not address the needs of recent technology. Nowadays, effective active heat transfer methods like ultrasonic vibration have been explored by Delouei et al. [1]. Another mechanism involves adding nanoparticles to the base fluid to improve heat transfer; this approach, discussed by Siavashi et al. [2], utilizes nanoparticles, known as nanofluids, to overcome this deficiency. At present, a widely explored research area for enhancing the thermal conductivity of base fluids is nanotechnology, as investigated by Izadi et al. [3]. The nanofluids have widespread applications in various engineering and industrial processes. Applications of this nature encompass cooling systems, heat exchangers, geothermal and solar energy systems, and

biomedicine, particularly in the realm of targeted drug delivery, as highlighted by Siavashi et al. [2]. A considerable number of researchers have discussed the flows of nanofluid and its applications [2–7]. Akmal et al. [8] observed that the heat transfer rate increases as the values of the thermophoresis parameter increase. Zeeshan et al. [9] analyzed a convective MHD nanofluid water/ethylene glycol based flow towards a vertical cone. Hady et al. [10] reported a rapid reduction in heat transfer rates due to an increase in the nanofluid's temperature and the solid volume fraction. Liu et al. [11] proposed a Pt/TiO_2 nanocomposite for cancer-cell treatment because noble metal nanoparticles are supposed to enhance the photocatalytic activity of TiO_2 nanoparticles. Some other significant studies for the reader's interest can be found in [12–17].

Nanoparticles such as *Cu*, *Ag*, and *Au* are not readily available and are expensive. Additionally, unmodified particles of *Cu*, *Ag*, and *Au* may pose potential toxicity risks, as highlighted by Parveen et al. [18]. The availability, cost, and potential toxicity of the particles, especially for unmodified mono nanofluid particles, will impact the manufacturing cost of production and pose health risks. Researchers have established a novel generation of heat transfer fluid as an extension towards nanofluid technology. This involves two or more dilute suspensions of composite nanoparticles in a base fluid, giving rise to a new class of fluid called hybrid nanofluids, as discussed by Chahregh et al. [19]. These hybrid nanofluids overcome limitations and simultaneously enhance the physical and chemical properties of the materials involved. The investigation into the temperature-dependent viscosity and thermal conductivity of hybrid nanofluid over a rotating vertical cone is vital for advancing our understanding of nanofluid dynamics, optimizing industrial processes, and exploring the potential of nanotechnology in heat transfer applications.

The behaviour of a hybrid nanofluid composed of TiO_2 and *Ag* in pure blood was studied by Chahregh et al. [19]. They reported the asymmetry of the channel, caused by different permeability at walls, significantly affects the nature of flow. A numerical investigation of the impact of magnetic field localization on the vortex generation in hybrid nanofluid flow studied by Ali et al. [20]. Many other investigations related to hybrid nanofluid have been published [21–23] to mention just a few.

It is known that many of the industrially and technologically important fluids are non-Newtonian fluids. In this article, a non-Newtonian micropolar fluid is considered. The most common type of non-Newtonian micropolar fluid is a fluid with a micro-structure that may consist of rigid, randomly oriented particles suspended in a viscous medium. *MHD* flow and heat transfer of carbon nanotube ($CNTs/H_2O$) nanoparticles suspended in micropolar dusty fluid, considering thermal radiation, was studied by Ghadikolaei et al. [24]. In this study, they reported that the thermal boundary layer thickness increases with increasing volume fraction of nanoparticles. Sandeep et al. [25] reported that hybrid ferroliquid and thermal radiation play a significant role in stream and energy transport in their study of radiative MHD dusty-hybrid ferrofluids, taking Fe_3O_4 and $CoFe_2O_4$ as nanoparticles in kerosene/water-based liquids. Several research studies on the flow of micropolar hybrid nanoliquids have been analyzed in the relevant literature [26–28].

Motivated by the aforementioned works, the present study extends the work of Malik et al. [29]. This extension is not a simple one as the authors aim to address a hybrid nanofluid with spin gradient viscosity for a non-Newtonian micropolar fluid, an aspect that was not covered in their study. Furthermore, this extension addresses a gap not explored in classical fluid dynamics, as far as our knowledge extends. We examine the effects of volumetric nanofractions, micropolar, and viscous fluids and compare their impacts.

2 Mathematical Formulation of the Problem

Consider an inverted isothermal rotating cone with a semi-vertical angle of Θ^* and time-dependent angular velocity of Ω. In this cone, a two-dimensional, incompressible, and unsteady magneto-micropolar hybrid nanofluid flow consisting of $Ag-MgO$ with a variable viscosity of μ_{hnf} and thermal conductivity of k_{hnf} with a reference length of L is surrounded by a porous medium. Additionally, heat transfer is incorporated at the surface of the inverted cone in the presence of thermal radiation effects. Buoyancy forces are present due to temperature variations, with the assumption that the surface of the permeable cone is held at a variable temperature of $T(x)$, where the temperature far away from the surface of the cone is denoted as T_∞. The graphical representation of the flow model is illustrated in Fig. 1. Under these assumptions, the governing equations [29,30] for the boundary layer flow takes the form:

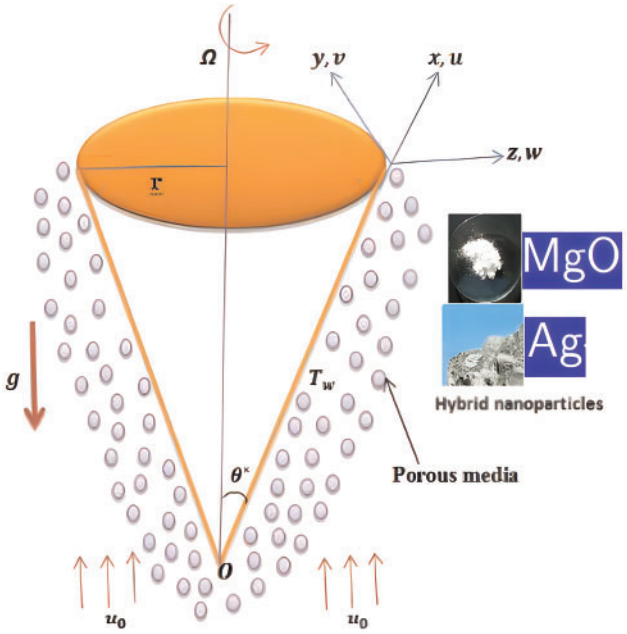

Figure 1: Geometry of the flow

$$\frac{\partial (xu)}{\partial x}+\frac{\partial (xv)}{\partial z}=0, \tag{1}$$

$$\frac{\partial u}{\partial t}+u\frac{\partial u}{\partial x}+w\frac{\partial u}{\partial z}-\frac{v^2}{x}=\frac{1}{\rho_{hnf}}\frac{\partial}{\partial z}\left[(\mu_{hnf}+\kappa)\left(\frac{\partial u}{\partial z}\right)\right]+\kappa\frac{\partial N}{\partial z}-\frac{\nu_{hnf}}{K_0}u$$
$$+g^*(\beta_T)_{hnf}(T-T_\infty)\cos\Theta^*-\frac{\sigma_{hnf}B_0^2}{\rho_{hnf}}u, \tag{2}$$

$$\frac{\partial v}{\partial t}+u\frac{\partial v}{\partial x}+w\frac{\partial v}{\partial z}+\frac{uv}{x}=\frac{1}{\rho_{hnf}}\frac{\partial}{\partial z}\left[(\mu_{hnf}+\kappa)\left(\frac{\partial v}{\partial z}\right)\right]+\kappa\frac{\partial N}{\partial z}-\frac{\nu_{hnf}}{K_0}v-\frac{\sigma_{hnf}B_0^2}{\rho_{hnf}}v, \tag{3}$$

$$\frac{\partial N}{\partial t}+u\frac{\partial N}{\partial x}+w\frac{\partial N}{\partial z}=\frac{\gamma_{hnf}}{\rho_{hnf}j}\frac{\partial^2 N}{\partial z^2}-\kappa\left(2N+\frac{\partial u}{\partial z}\right), \tag{4}$$

$$\frac{\partial T}{\partial t}+u\frac{\partial T}{\partial x}+w\frac{\partial T}{\partial z}=\frac{1}{(\rho C_p)_{hnf}}\frac{\partial}{\partial z}\left(k_{hnf}\frac{\partial T}{\partial z}\right)-\frac{1}{(\rho C_p)_{hnf}}\frac{\partial q_r}{\partial z}, \tag{5}$$

where $q_r=\dfrac{16T_\infty^3\sigma^*}{3k^*}\left(\dfrac{\partial T}{\partial z}\right)$ [31], $r=x\cos\Theta^*$ and, μ_{hnf} and k_{hnf} depend on temperature as defined [29]:

$$\mu_{hnf}=\mu_0(1-A\theta(\eta)),\quad k_{hnf}=k_0(1+\zeta\theta(\eta)). \tag{6}$$

$A<0$ for gas and $A>0$ for liquid, $A=\chi(T_w-T_\infty)$ and $\zeta=-c(T_w-T_\infty)$, where χ and c are arbitrary constants. The initial and boundary conditions are given by:

$$t\le 0,\quad u=0,\quad v=0,\quad w=0,\quad N=0,\quad T=T_0\quad \forall(x,y,z), \tag{7a}$$

$$t>0,\quad u=0,\quad v=\frac{1}{1-At^*}\Omega x\sin\Theta^*,\quad N=0,\quad T=T_w,\quad \text{at}\quad z=0, \tag{7b}$$

$$u\to 0,\quad v\to 0,\quad N\to 0,\quad T\to 0,\quad \text{as}\quad z\to\infty, \tag{7c}$$

where $t^*=\Omega t\sin\Theta^*$. All the values for the parameters Cp, K, ρ, β, σ, α are taken from Table 1. (Hiba et al. [32]).

Table 1: Experimental values of basis fluid and nanoparticles

Property	C_p (J/kg K)	k (W/mk)	ρ (kg/m^3)	$\beta\times10^{-5}$	σ (s/m)	α (m^2/s)
H_2O	4179	0.613	997.1	21	5.5×10^{-6}	1.47×10^{-7}
Ag	235	429	10,500	5.4	8.1×10^{-4}	147×10^{-3}
MgO	879	30	3970	3.36	8×10^{-4}	95.3×10^{-7}

According to Khan et al. [33], volume fraction, thermal conductivity, density, heat capacitance, thermal expansion coefficient, thermal conductivity and viscosity of the hybrid nanofluid, are defined by Eqs. (8)–(14), respectively:

$$\phi=\phi_{Ag}+\phi_{MgO}, \tag{8}$$

$$\alpha_{hnf}=\frac{k_{hnf}}{(\rho)_{hnf}}, \tag{9}$$

$$\rho_{hnf}=(1-\phi)\rho_f+(\phi_{Ag}\times\rho_{Ag}+\phi_{MgO}\times\rho_{MgO}), \tag{10}$$

$$(\rho C_p)_{hnf}=(1-\phi)(\rho C_p)_f+(\phi_{Ag}\times(\rho C_p)_{Ag}+\phi_{MgO}\times(\rho C_p)_{MgO}), \tag{11}$$

$$(\rho\beta)_{hnf}=(1-\phi)(\rho\beta)_f+(\phi_{Ag}\times(\rho\beta)_{Ag}+\phi_{MgO}\times(\rho\beta)_{MgO}), \tag{12}$$

$$\frac{k_{hnf}}{k_{bf}}=\frac{k_{MgO}+2k_{bf}+2\phi_{MgO}(k_{MgO}-k_{bf})}{k_{MgO}+2k_{bf}-\phi_{MgO}(k_{MgO}-k_{bf})},\quad \frac{k_{bf}}{k_f}=\frac{k_{Ag}+2k_f+2\phi_{Ag}(k_{Ag}-k_f)}{k_{Ag}+2k_f-\phi_{Ag}(k_{Ag}-k_f)} \tag{13}$$

$$\mu_{hnf} = \frac{\mu_f}{(1-(\phi_{Ag}+\phi_{MgO}))^{2.5}}. \tag{14}$$

Using Eqs. (6), (8)–(14) and the transformations specified by [29]:

$$u = -\frac{\Omega x \sin\Theta^*}{2(1-At^*)} f'(\eta), \quad v = \frac{\Omega x \sin\Theta^*}{1-At^*} g(\eta), \quad w = \left(\frac{\Omega x \sin\Theta^*}{1-At^*}\right)^{1/2} f(\eta)$$

$$N = \frac{x}{2}\left(\frac{\nu_f \Omega \sin\Theta^*}{1-At^*}\right)^{1/2} \omega(\eta), \quad T = T_\infty + (T_w - T_\infty)\theta(\eta), \quad T_w - T_\infty = \frac{(T_0 - T_\infty)}{(1-At^*)}\frac{x}{L}$$

$$\eta = \left(\frac{\Omega \sin\Theta^*}{\nu_0(1-At^*)}\right)^{1/2} z,$$

the system of partial differential Eqs. (1)–(5) is transformed into ordinary differential Eqs. (15)–(18):

$$(1 - A\theta + \phi_1 K) f''' - [A\theta' + K] f'' + \phi_1\phi_2 \left[\frac{1}{2} f'^2 - f f'' - 2g^2 - s(f' + \frac{\eta}{2} f'') - 2\phi_4 \lambda\theta\right] + \phi_2[K\omega - K_p f' + \phi_3 M f'] = 0, \tag{15}$$

$$(1 - A\theta + \phi_1 K)\, g'' - [A\theta' + K] g' + \phi_1\phi_2 \left[g f' - f g' - s\left(g + \frac{\eta}{2} g'\right)\right] - \phi_2[K_p g + \phi_3 M g] = 0, \tag{16}$$

$$\left(1 - A\theta + \frac{1}{2}\phi_1 K\right)\omega'' - \left[A\theta' + \frac{1}{2}K\right]\omega' + \phi_1\phi_2\left[\omega f' - f\omega' - s\left(\omega + \frac{\eta}{2}\omega'\right)\right] - \phi_2 K B(2\omega - f'') = 0, \tag{17}$$

$$\frac{k_{hnf}}{k_f}\left(\frac{1}{Pr}\right)[(1 + \varepsilon\theta + Rd)\theta'' + \varepsilon\theta'^2] + \phi_5\left[\frac{1}{2}\theta f' - f\theta' - s\left(2\theta + \frac{\eta}{2}\theta'\right)\right] = 0, \tag{18}$$

where

$$Gr = g^*(T_0 - T_\infty)\frac{L^3}{\nu_f^2}\cos\Theta^*, \quad Re_L = \frac{\Omega L^2 \sin\Theta^*}{\nu_f}, \quad \lambda = \frac{Gr}{Re_L}, \quad K = \frac{\kappa}{\mu_f}, \quad B = \frac{\nu_f(1-st^*)}{j\Omega\sin\Theta^*},$$

$$Rd = \frac{16\sigma^* T_\infty^3 L^2}{3k^* Gr^{1/2}\mu_f(\rho C_p)_f}, \quad M = \frac{\sigma_f B_0^2(1-st^*)}{\Omega\sin\Theta^*\rho_f}, \quad k_p = \frac{\nu_f(1-st^*)}{k_0\Omega\sin\Theta^*}, \quad Pr = \frac{\nu_{(}\rho C_p)_f}{k_f},$$

$$\phi_1 = (1-\phi) + \phi_{Ag}\left(\frac{\rho_{Ag}}{\rho_f}\right) + \phi_{MgO}\left(\frac{\rho_{MgO}}{\rho_f}\right), \quad \phi_2 = (1-\phi)^{1/2}, \quad \phi_3 = \frac{\sigma_{hnf}}{\sigma_f},$$

$$\phi_4 = (1-\phi) + \phi_{Ag}\left(\frac{(\beta_t)_{Ag}}{(\beta_t)_f}\right) + \phi_{MgO}\left(\frac{(\beta_t)_{MgO}}{(\beta_t)_f}\right),$$

$$\phi_5 = (1-\phi) + \phi_{Ag}\left(\frac{(\rho C_p)_{Ag}}{(\rho C_p)_f}\right) + \phi_{MgO}\left(\frac{(\rho C_p)_{MgO}}{(\rho C_p)_f}\right).$$

The nondimensional boundary conditions take the form:

$$f(0) = 0, \quad f'(0) = 0, \quad g(0) = 1, \quad \omega(0) = 0, \quad \theta(0) = 1, \tag{19a}$$

$$f' \to 0, \quad g \to 0, \quad \omega \to 0, \quad \theta \to 0 \quad \text{as} \quad \eta \to \infty. \tag{19b}$$

The skin friction coefficient and local Nusselt number are defined as:

$$C_{fx} = \frac{2\tau_{xz}}{\rho_f(\frac{\Omega x \sin\Theta^*}{1-st^*})^2}, \quad C_{fy} = \frac{-2\tau_{yz}}{\rho_f(\frac{\Omega x \sin\Theta^*}{1-st^*})^2} \tag{20}$$

$$Nu_x = -\frac{xq_w}{k_f(T_w - T_\infty)} \tag{21}$$

where

$$\tau_{xz} = \mu_{hnf}\left(\frac{\partial u}{\partial z}\right)_{z=0}, \quad \tau_{yz} = \mu_{hnf}\left(\frac{\partial v}{\partial z}\right)_{z=0}, \quad q_w = -\frac{x}{k_f(T_w - T_\infty)}\left[k_{hnf}\frac{\partial T}{\partial z} + (q_r)_w\right]_{z=0} z.$$

The corresponding non-dimensional form for Eqs. (20) and (21) are as follows:

$$C_{fx}Re_x^{1/2} = -\left[\frac{1}{\phi_2}(1 - A\theta)f''(\eta)\right]_{\eta=0}, \quad C_{fy}Re_x^{1/2} = -\left[\frac{2}{\phi_2}(1 - A\theta)g'(\eta)\right]_{\eta=0} \tag{22}$$

$$Nu_x Re_x^{-1/2} = -\left(\frac{k_{hnf}}{k_f} + Rd\right)\theta'(0), \tag{23}$$

where $Re_x = \dfrac{x^2\Omega \sin\Theta^*}{\nu_f(1 - st^*)}$ is the Reynolds number.

3 Numerical Method

Numerical solutions to the non-dimensionalized system of Eqs. (15)–(18) are obtained using the *OGMDSQLM*, proposed by Mkhatshwa [34]. The numerical solutions were generated through codes developed in MATLAB. The solution algorithm of this numerical method is based on numerical techniques namely *QLM*, spectral collocation, multidomain overlapping grid and Lagrange interpolation polynomials with Gauss-Lobatto-Chebyshev grid points. To implement the method, the integration domain, $[0, \eta_\infty]$, is divided into finite overlapping subintervals of equal length, illustrated in Fig. 2. As shown in Fig. 2, the domain of integration is divided into $p \in \mathbb{N}|p > 1$ subintervals. Each subinterval is then discretized into a predefined number of collocation points, say $N_\eta + 1$, where η denotes a space variable. The *SQLM* is then applied in each subinterval, with the approximate solution(s) of a previous subinterval set as starting values for *SQLM* iterations in the next interval. The incorporation of the overlapping phenomenon is achieved by permitting an iterative process within the current subinterval, wherein each iteration induces a displacement, denoted as a fixed step ($\eta_0^2 - \eta_0^1$, as seen in Fig. 2). To obtain the solution of the nonlinear system of differential Eqs. (15)–(18) employing the overlapping grid multidomain spectral quasilinearization method, the algorithm is as follows: firstly, the division of the integration interval into overlapping subintervals, as illustrated in Fig. 2; subsequently, the application of *QLM* as proposed by Motsa et al. [35] to Eqs. (24)–(27) where l signifies a subinterval, and $(r+1)$ denotes the current iteration level; further, the computation of derivatives at each subinterval collocation point through the utilization of the Chebyshev numerical differentiation matrix; and the employment of the pseudospectral collocation method at the boundaries (Eq. (34)). Ultimately, an

iterative solution is obtained through the resolution of a matrix equation, as given by Eqs. (33) and (34), yielding the approximate solution.

$$a^{1,l}_{1,1} f'_{l,(r+1)} + a^{2,l}_{1,1} f''_{l,(r+1)} + a^{3,l}_{1,1} f'''_{l,(r+1)} + a^{0,l}_{1,1} f + a^{1,l}_{1,4} \theta'_{l,(r+1)} + a^{0,l}_{1,4} \theta_{l,(r+1)} = R_{1,l} \tag{24}$$

$$a^{1,l}_{2,2} g'_{l,(r+1)} + a^{2,l}_{2,2} g''_{l,(r+1)} + a^{1,l}_{2,4} \theta'_{l,(r+1)} + a^{0,l}_{2,4} \theta + a^{1,l}_{2,1} f'_{l,(r+1)} + a^{0,l}_{2,1} f_{l,(r+1)} = R_{2,l} \tag{25}$$

$$\begin{aligned} &a^{1,l}_{3,3} \omega'_{l,(r+1)} + a^{2,l}_{3,3} \omega'' _{l,(r+1)} + a^{0,l}_{3,3} \omega_{l,(r+1)} + a^{1,l}_{3,4} \theta' + a^{0,l}_{3,4} \theta_{l,(r+1)} + a^{1,l}_{3,1} f'_{l,(r+1)} \\ &\quad + a^{2,l}_{3,1} f''_{l,(r+1)} + a^{0,l}_{3,1} f_{l,(r+1)} = R_{3,l} \end{aligned} \tag{26}$$

$$a^{1,l}_{4,4} \theta'_{l,(r+1)} + a^{2,l}_{4,4} \theta''_{l,(r+1)} + a^{0,l}_{4,4} \theta_{l,(r+1)} + a^{1,l}_{4,1} f' + a^{0,l}_{4,1} f_{l,(r+1)} = R_{4,l} \tag{27}$$

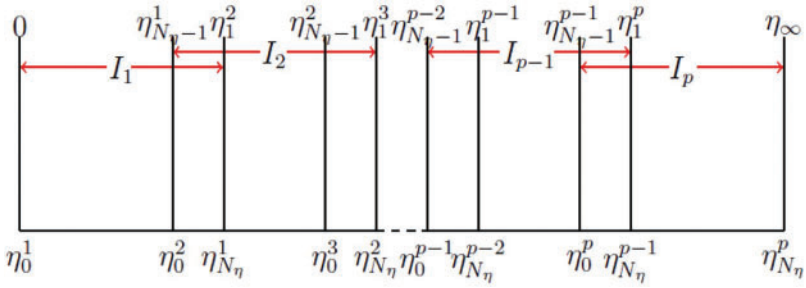

Figure 2: Overlapping grid, Mkhasthwa [34]

Using the *SQLM* method proposed by Motsa et al. [35], the coefficients of the unknowns are evaluated at the previous iteration level r (see Eqs. (28) and (29)).

$$\left.\begin{aligned} &a^{1,l}_{1,1} = \phi_1\phi_2 f'_{l,r} - \phi_1\phi_2 s - \phi_2 K_p + \phi_2\phi_3 M, \quad a^{(2,l)}_{1,1} = -A\theta'_{l,r} - K - \phi_1\phi_2 f_{l,r} - \phi_1\phi_2 s\tfrac{\eta}{2} \\ &a^{3,l}_{1,1} = 1 - A\theta_{l,r} + \phi_1 K, \quad a^{(0,l)}_{1,1} = -\phi_1\phi_2 f''_{l,r}, \quad a^{(1,l)}_{1,4} = -Af''_{l,r}, \quad a^{0,l}_{1,4} = -Af'''_{l,r} - 2\phi_1\phi_2\phi_4 K \\ &a^{(0,l)}_{2,2} = \phi_1\phi_2 f'_{l,r} - \phi_1\phi_2 s - \phi_2 k_p - \phi_2\phi_3 M, \quad a^{(1,l)}_{2,2} = -A\theta'_{l,r} - K - \phi_1\phi_2 f_{l,r} - \phi_1\Phi_2 s\tfrac{\eta}{2} \\ &a^{2,l}_{2,2} = 1 - A\theta l, r + \phi_1 K, \quad a^{(0,l)}_{2,2} = \phi_1\phi_2 f'_{l,r} - \phi_1\phi_2 s - \phi_2 K_p - \phi_2\phi_3 M, \quad a^{1,l}_{2,4} = -Ag'_{l,r}, \\ &a^{(0,l)}_{2,4} = -Ag''_{l,r}, \quad a^{(1,l)}_{2,1} = \phi_1\phi_2 g_{l,r}, \quad a^{0,l}_{2,1} = -\phi_1\phi_2 g'_{l,r}, \quad a^{(1,l)}_{3,3} = -A\theta'_{l,r} - 0.5K - \phi_1\phi_2 f_{l,r} - \phi_1\phi_2\frac{\eta}{2}, \end{aligned}\right\} \tag{28}$$

$$\left.\begin{aligned} &a^{2,l}_{3,3} = 1 - A\theta_{l,r} + 0.5\phi_1 K, \quad a^{(0,l)}_{3,3} = \phi_1\phi_2 f'_{l,r} - \phi_1\phi_2 s - 2KB\phi_2, \quad a^{1,l}_{3,4} = -A\omega'_{l,r}, \\ &a^{0,l}_{3,4} = -A\omega''_{l,r}, \quad a^{(1,l)}_{3,1} = \phi_1\phi_2\omega_{l,r}, \quad a^{0,l}_{3,4} = -A\omega''_{l,r}, \\ &a^{2,l}_{3,1} = \phi_2 KB, \quad a^{(0,l)}_{3,1} = -\phi_1\phi_2\omega'_{l,r}, \quad a^{(1,l)}_{4,4} = 2\varepsilon\theta'_{l,r}\tfrac{K_{hnf}}{K_f P_r} - \phi_5 f_{l,r} - \phi_5 s\frac{\eta}{2}, \\ &a^{2,l}_{4,4} = \tfrac{K_{hnf}}{K_f P_r}(1 + \eta\theta_{l,r} + Rd), \quad a^{0,l}_{4,4} = \tfrac{K_{hnf}}{K_f P_r}\eta\theta''_{l,r} + 0.5\phi_5 f'_{l,r} - 2\phi_5 s, \\ &a^{1,l}_{4,1} = 0.5\phi_5\theta_{l,r}, \quad a^{(0,l)}_{4,1} = -\phi_5\theta'_{l,r}. \end{aligned}\right\} \tag{29}$$

As mentioned earlier, the essence of the overlapping grid multidomain spectral quasilinearization is the slicing of the physical domain into a finite number of overlapping subintervals, the non-dimensional boundary conditions then become as written in Eq. (30).

$$f(0)_{l,(r+1)} = 0, \quad f'(0)_{l,(r+1)} = 0, \quad g(0)_{l,(r+1)} = 1, \quad \omega(0)_{l,(r+1)} = 0, \quad \theta(0)_{l,(r+1)} = 1, \tag{30a}$$

$$f'_{l,(r+1)} \to 0, \quad g_{l,(r+1)} \to 0, \quad \omega_{l,(r+1)} \to 0, \quad \theta_{l,(r+1)} \to 0 \quad \text{as} \quad \eta \to \infty. \tag{30b}$$

The linearized system of Eqs. (24)–(27) can be written compactly as shown in system (31), where $\mathbf{D}$ is the Chebyshev numerical differentiation matrix, $\mathbf{I}$ is the identity matrix of dimension equal to the number of collocation points. Furthermore, the linearization coefficients, for example $a_{1,1}^{(1,l)}$, are diagonal matrices of dimension equal to number of collocation points.

$$\left.\begin{aligned}
&\left[a_{1,1}^{(1,l)}\mathbf{D}^1 + a_{1,1}^{(2,l)}\mathbf{D}^2 + a_{1,1}^{(3,l)}\mathbf{D}^3 + a_{1,1}^{(0,l)}\mathbf{I}\right]\mathbf{F}_{l,(r+1)} + \left[a_{1,4}^{(1,l)}\mathbf{D} + a_{1,4}^{(0,l)}\mathbf{I}\right]\Theta_{l,(r+1)} = \mathbf{R}_{1,l},\\
&\left[a_{2,2}^{(1,l)}\mathbf{D} + a_{2,2}^{(2,l)}\mathbf{D}^2 + a_{2,2}^{(0,l)}\mathbf{I}\right]\mathbf{G}_{l,(r+1)} + \left[a_{2,4}^{(1,l)}\mathbf{D} + a_{2,4}^{(0,l)}\mathbf{I}\right]\Theta_{l,(r+1)}\\
&\quad + \left[a_{2,1}^{(1,l)}\mathbf{D} + a_{2,1}^{(0,l)}\mathbf{I}\right]\mathbf{F}_{l,(r+1)} = \mathbf{R}_{2,l},\\
&\left[a_{3,3}^{(1,l)}\mathbf{D} + a_{3,3}^{(2,l)}\mathbf{D}^2 + a_{3,3}^{(0,l)}\mathbf{I}\right]\Omega_{l,(r+1)} + \left[a_{3,4}^{(1,l)}\mathbf{D} + a_{3,4}^{(0,l)}\mathbf{I}\right]\Theta_{l,(r+1)}\\
&\quad + \left[a_{3,1}^{(1,l)}\mathbf{D} + a_{3,1}^{(2,l)}\mathbf{D}^2 + a_{3,1}^{(0,l)}\mathbf{I}\right]\mathbf{F}_{l,(r+1)} = \mathbf{R}_{3,l},\\
&\left[\alpha_{4,4}^{(1,l)}\mathbf{D} + \alpha_{4,4}^{(2,l)}\mathbf{D}^2 + \alpha_{4,4}^{(0,l)}\mathbf{I}\right]\Theta_{l,(r+1)} + \left[\alpha_{4,1}^{(1,l)}\mathbf{D} + \alpha_{4,1}^{(0,l)}\mathbf{I}\right]\mathbf{F}_{l,(r+1)} = R_{4,l}.
\end{aligned}\right\} \tag{31}$$

The system of Eq. (31) can be represented in matrix from as system (32). The column vectors of unknowns at a subinterval and current iteration level are: $\mathbf{F}_{r+1}^{l}$, $\mathbf{G}_{r+1}^{l}$, Ω_{r+1}^{l},Θ_{r+1}^{l}.

$$\begin{bmatrix} A_{11} & A_{12} & A_{13} & A_{14} \\ A_{21} & A_{22} & A_{23} & A_{24} \\ A_{31} & A_{32} & A_{33} & A_{34} \\ A_{41} & A_{42} & A_{43} & A_{44} \end{bmatrix} \begin{bmatrix} \mathbf{F}_{r+1}^{l} \\ \mathbf{G}_{r+1}^{l} \\ \Omega_{r+1}^{l} \\ \Theta_{r+1}^{l} \end{bmatrix} = \begin{bmatrix} \mathbf{R}_{1}^{l} \\ \mathbf{R}_{2}^{l} \\ \mathbf{R}_{3}^{l} \\ \mathbf{R}_{4}^{l} \end{bmatrix} \tag{32}$$

where

$$A_{11} = \left[a_{1,1}^{(1,l)}\mathbf{D} + a_{1,1}^{(2,l)}\mathbf{D}^2 + a_{1,1}^{(3,l)}\mathbf{D}^3 + a_{1,1}^{(0,l)}\mathbf{I}\right], \quad A_{12} = \mathbf{0}, \quad A_{13} = \mathbf{0}, \quad A_{14} = \left[a_{1,4}^{(1,l)}\mathbf{D} + a_{1,4}^{(0,l)}\mathbf{I}\right],$$

$$A_{21} = \left[a_{2,1}^{(1,l)}\mathbf{D} + a_{2,1}^{(0,l)}\mathbf{I}\right], \; A_{22} = \left[a_{2,2}^{(1,l)}\mathbf{D}^2 + a_{2,2}^{(2,l)}\mathbf{D} + a_{2,2}^{(0,l)}\mathbf{I}\right], \; A_{23} = \mathbf{0}, \quad A_{24} = \left[a_{2,4}^{(1,l)}\mathbf{D} + a_{2,4}^{(0,l)}\mathbf{I}\right],$$

$$A_{31} = a_{3,1}^{(1,l)}\mathbf{D}^2 + a_{3,1}^{(1,l)}\mathbf{D} + a_{3,l}^{(0,l)}\mathbf{l}, \quad A_{32} = \mathbf{0}, \quad A_{33} = \left[a_{3,3}^{(1,l)}\mathbf{D} + a_{3,3}^{(2,l)}\mathbf{D}^2 + a_{3,3}^{(0,l)}\mathbf{I}\right], \quad A_{34} = \left[a_{3,4}^{(1,l)}\mathbf{D} + a_{3,4}^{(0,l)}\mathbf{I}\right],$$

$$A_{41} = \left[\alpha_{4,1}^{(1)}\mathbf{D} + \alpha_{4,1}^{(0)}\mathbf{I}\right], \quad A_{42} = \mathbf{0}, \quad A_{43} = \mathbf{0}, \quad A_{44} = \left[\alpha_{4,4}^{(1,l)}\mathbf{D} + \alpha_{4,4}^{(2,l)}\mathbf{D}^2 + \alpha_{4,1}^{(0,l)}\mathbf{I}\right]. \tag{33}$$

and $\mathbf{0}$ is a square matrix of zeros, also of dimension consistent with the number of collocation points in the computation.

Applying the pseudospectral method at the boundaries gives:

$$\left.\begin{aligned} f_{r+1}(z_{N_\eta}) = 0, \quad \sum_{j=0}^{N_\eta} D_{N,j} f_{j,(r+1)} = 0, \quad g_{r+1}(z_{N_\eta}) = 1, \\ \omega_{r+1}(z_{N_\eta}) = 0, \quad \theta_{r+1}(z_{N_\eta}) = 1 \quad \text{at} \quad \eta = 0. \\ \sum_{j=0}^{N_\eta} D_{0,j} f_{j,(r+1)}(z_0) \to 0, \quad g_{j,(r+1)}(z_0) \to 0, \\ \omega_{j,(r+1)}(z_0) \to 0, \quad \theta_{j,(r+1)}(z_0) \to 0, \quad \text{as} \quad \eta \to \infty. \end{aligned}\right\} \tag{34}$$

The *OGMDSQLM* leads to a sparse form of the coefficient matrix in system (32), which is expressed in its expanded form below, with the boundary conditions incorporated accordingly on the diagonal submatrices.

$$\left[\begin{array}{cccccc|cccccc|cccccc|cccccc}
\mathbf{D}_{0,0} & \mathbf{D}_{0,1} & \mathbf{D}_{0,2} & \dots & \dots & \mathbf{D}_{0,N} & 0 & 0 & \dots & \dots & 0 & 0 & 0 & \dots & \dots & 0 & 0 & 0 & \dots & \dots & 0 \\
 & & & & & & & & & & & & & & & & & & & & \\
 & & \mathbf{A}_{11} & & & & & & \mathbf{A}_{12} & & & & & \mathbf{A}_{13} & & & & & \mathbf{A}_{14} & & \\
 & & & & & & & & & & & & & & & & & & & & \\
\mathbf{D}_{N,0} & \mathbf{D}_{N,1} & \mathbf{D}_{N,2} & \dots & \dots & \mathbf{D}_{N,N} & 0 & 0 & \dots & \dots & 0 & 0 & 0 & \dots & \dots & 0 & 0 & 0 & \dots & \dots & 0 \\
0 & 0 & 0 & \dots & \dots & 1 & 0 & 0 & \dots & \dots & 0 & 0 & 0 & \dots & \dots & 0 & 0 & 0 & \dots & \dots & 0 \\
\hline
0 & 0 & 0 & \dots & \dots & 0 & 1 & 0 & \dots & \dots & 0 & 0 & 0 & \dots & \dots & 0 & 0 & 0 & \dots & \dots & 0 \\
 & & & & & & & & & & & & & & & & & & & & \\
 & & \mathbf{A}_{21} & & & & & & \mathbf{A}_{22} & & & & & \mathbf{A}_{23} & & & & & \mathbf{A}_{24} & & \\
 & & & & & & & & & & & & & & & & & & & & \\
0 & 0 & 0 & \dots & \dots & 0 & 0 & 0 & \dots & \dots & \mathbf{1} & 0 & 0 & \dots & \dots & 0 & 0 & 0 & \dots & \dots & 0 \\
\hline
0 & 0 & 0 & \dots & \dots & 0 & 0 & 0 & \dots & \dots & 0 & 1 & 0 & \dots & \dots & 0 & 0 & 0 & \dots & \dots & 0 \\
 & & & & & & & & & & & & & & & & & & & & \\
 & & \mathbf{A}_{31} & & & & & & \mathbf{A}_{32} & & & & & \mathbf{A}_{33} & & & & & \mathbf{A}_{34} & & \\
 & & & & & & & & & & & & & & & & & & & & \\
0 & 0 & 0 & \dots & \dots & 0 & 0 & 0 & \dots & \dots & 0 & 0 & 0 & \dots & \dots & 1 & 0 & 0 & \dots & \dots & 0 \\
\hline
0 & 0 & 0 & \dots & \dots & 0 & 0 & 0 & \dots & \dots & 0 & 1 & 0 & \dots & \dots & 0 & 1 & 0 & \dots & \dots & 0 \\
 & & & & & & & & & & & & & & & & & & & & \\
 & & \mathbf{A}_{41} & & & & & & \mathbf{A}_{42} & & & & & \mathbf{A}_{43} & & & & & \mathbf{A}_{44} & & \\
 & & & & & & & & & & & & & & & & & & & & \\
0 & 0 & 0 & \dots & \dots & 0 & 0 & 0 & \dots & \dots & 0 & 0 & 0 & \dots & \dots & 0 & 0 & 0 & \dots & \dots & 1
\end{array}\right] \tag{35}$$

To begin the iterative search for approximate solutions, the following functions:

$$f_0(\eta) = \eta^2 \exp(-\eta), \quad g_0(\eta) = \exp(-\eta), \quad \omega_0(\eta) = \eta \exp(-\eta) \quad \text{and} \quad \theta_0(\eta) = \exp(-\eta), \tag{36}$$

that satisfy the boundary conditions are taken as approximate solutions.

4 Results and Discussion

To check the validity of the current numerical scheme, a comparison of the present values of skin friction and Nusselt number with those published in the literature by Malik et al. [29], Chamkha et al. [36] is presented in Table 2. Using the nanoparticle volume fractions of hybrid nanofluid consisting of portions of nano particles $\phi_{Ag} = 0.018$ and $\phi_{Mgo} = 0.002$, we examined the components of velocities, microrotation and temperature profile for selected parameters from the

following respective ranges $0 \leq \varepsilon \leq 0.5, 0 \leq s \leq 0.5, 0 \leq B \leq 3, 0 \leq A \leq 2.5, 0 \leq M \leq 1, 0 \leq Rd \leq 1$, $0 \leq K \leq 1, 0 \leq \lambda \leq 5$ which lead to convergence and stable results. The following parametric values are used for the numerical computations: $Pr = 6.8$, $\varepsilon = 0.2$, $s = 0.2$, $B = 2$, $A = 0.02$, $M = 0.5$, $K = 0.6$, $\lambda = 3$. As the value of the nondimentional form K, of the coupling number κ approaches one the fluid is more micropolar whereas as it approaches zero the fluid becomes more viscous. Fig. 3a shows that with an increase in the value of the coupling number, the fluid becomes more micropolar, resulting in a primary velocity slowdown in the vicinity of the boundary at its peak. Conversely, a decrease in velocity for the secondary flow is observed, as depicted in Fig. 3b. Physically this is due the rotational effect of the flow, the main flow is retarded and the secondary flow increases. Also, it can be observed from Fig. 3b, that the hybrid nanofluid, $\phi_{Ag} + \phi_{MgO}$, enhances the primary velocity than the mono-nanofluid ϕ_{MgO}. From Fig. 3b the reverse trend from the primary flow is observed throughout the flow medium. From Fig. 3c, it is observed that the hybrid nanoflid reduces the temperature compared to the mono-nanoflluid. This is because hybridizing appropriately chosen nanoparticles, the heat transfer of the particles in the medium increases. From the same figure it is seen micropolar fluids enhances the temperature. From Fig. 3d, the rotational effect in the fluid particles is observed by enhancing the micropolar parameter. When $K = 0$, there is no rotation, and consequently, no flow for ω, indicating that the fluid behaves as a viscous fluid. Moreover, from the same graph, it is observed the rotational effect for hybrid nanofluid near the boundary is greater than that of the mono-nanofluid. This may be due to the higher viscosity for hybrid nanofluid than the mono nanofluid which warrants further investigation.

Table 2: Numerical values for the skin friction for radiation and magnetic parameter for $\varepsilon = s = K_p = B = A = K = 0$

		Malik et al. [29]	Chamkha et al. [36]	Present
Pr	λ		$Re_x^{1/2} f''(0)$	
0.7	0	1.0253	1.0255	1.0254
0.7	1	2.2007	2012	2.2009
0.7	10	8.5041	8.5041	8.5042
			$Re_x^{-1/2} \theta'(0)$	
0.7	0	0.4295	0.4299	0.4297
0.7	1	0.6121	0.6120	0.6121
0.7	10	1.0097	1.0097	1.0098

Fig. 4a shows that the smaller the variable viscosity parameter, the more the primary velocity diminishes. Physically, this implies that in the higher viscous region (near the boundary), the dominant force is buoyancy, and an increase in nanofluid concentration leads to an increase in velocity. The more hybrid nanofluid, the higher the thermal conductivity, which allows an increase in Brownian motion and, consequently, particle energy transfer. It is also interesting to note that away from the vicinity of the boundary, in the free stream region, the reverse effect is observed. However, it is evident from Fig. 4b that an increase in the variable viscosity parameter results in a decreasing effect on the secondary flow. This is because as the coupling number K increases, the fluid becomes more micropolar, and consequently, the particle sniping effect significantly retards the secondary flow. For the fractional volume of the hybrid nanofluid, $\phi_{Ag} + \phi_{MgO}$, velocity is greater than the mon-nanofluid, ϕ_{MgO}, in both velocities. The influence of the variable viscosity parameter on temperature, presented

in Fig. 4c, indicates that the higher the variable viscosity parameter, the lower the temperature. It is also noted that fractional volume hybrid nanofluid, $\phi_{Ag} + \phi_{MgO}$, reduces the temperature than mon-nanofluid, ϕ_{MgO}. It is seen from the Fig. 4c that the temperature decreases with an increase in the variable viscosity parameter. It is also noted for fractional volume hybrid nanofluid, $\phi_{Ag} + \phi_{MgO}$, temperature decreases compared to the mon-nanofluid, ϕ_{MgO}. This is because more nanoparticles are involved the thermal properties of the resulting mixture are improved and Brownian motions of nanoparticles increases leading to increase the viscosity in the medium. Fig. 4d describes the effect of variable viscosity on microrotation, the hybrid nanofluid fraction is higher than the mon-nanofluid in the region closer to the vicinity of the boundary.

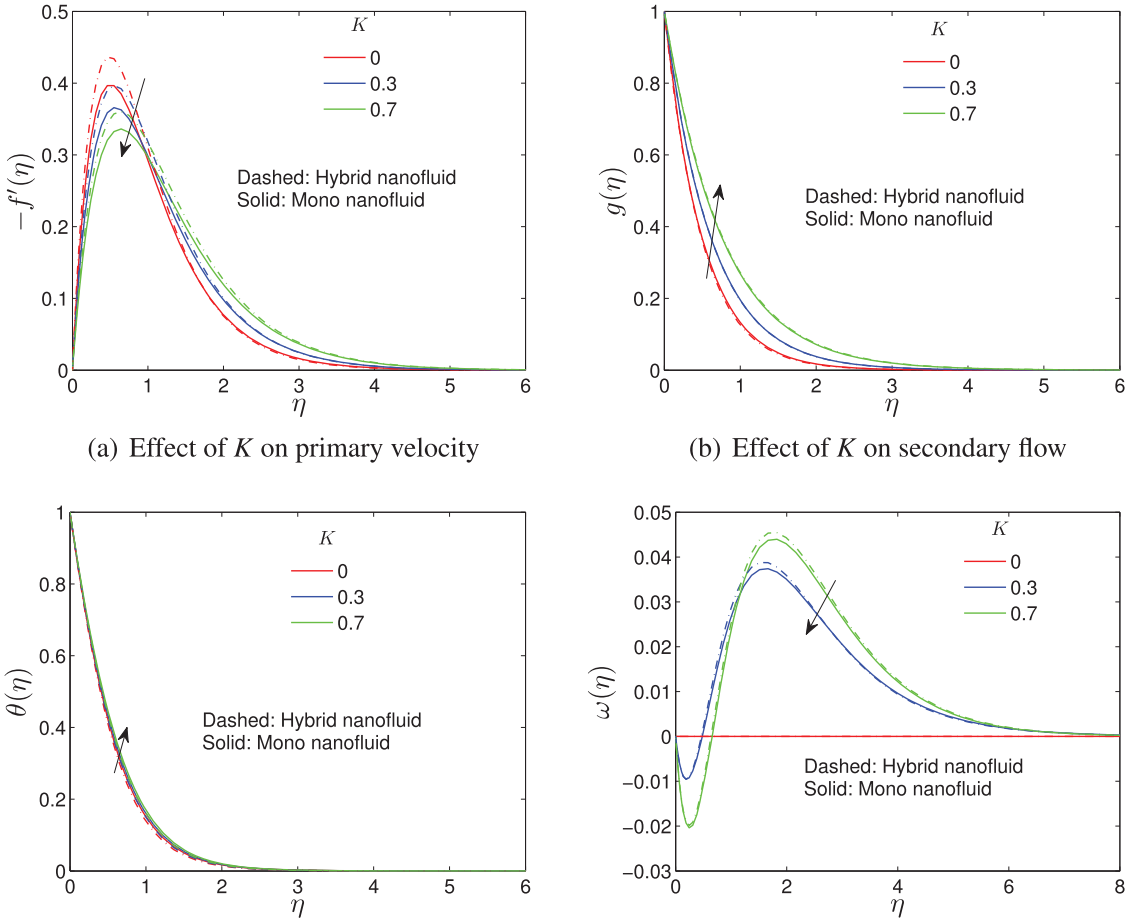

(a) Effect of K on primary velocity

(b) Effect of K on secondary flow

(c) Effect of K on temperatue

(d) Effect of K on microrotation

Figure 3: Coupling number effect

Fig. 5a,b shows the impact of porosity parameter on both primary and secondary flows. It is clear from the figures that primary velocity decreases with an increase in the porosity parameter. The velocities of the hybrid nanofluid, $\phi_{Ag} + \phi_{MgO}$, are enhanced as compared to the mono-nanofluid, ϕ_{MgO}. Physically increasing the value of k_0, that is less pour in the flow medium, in Eq. (2), and hence decreasing the value of K_p in Eq. (15) causes the porous zone's transparency to decrease and hence the velocity decreases. We can observe from these results hybrid nanofluid increase the flow velocities

than the mono-nanofluid. The effect of K_p on temperature and microrotation as shown in Fig. 5c,d is similar to the effect of K in Fig. 3c,d.

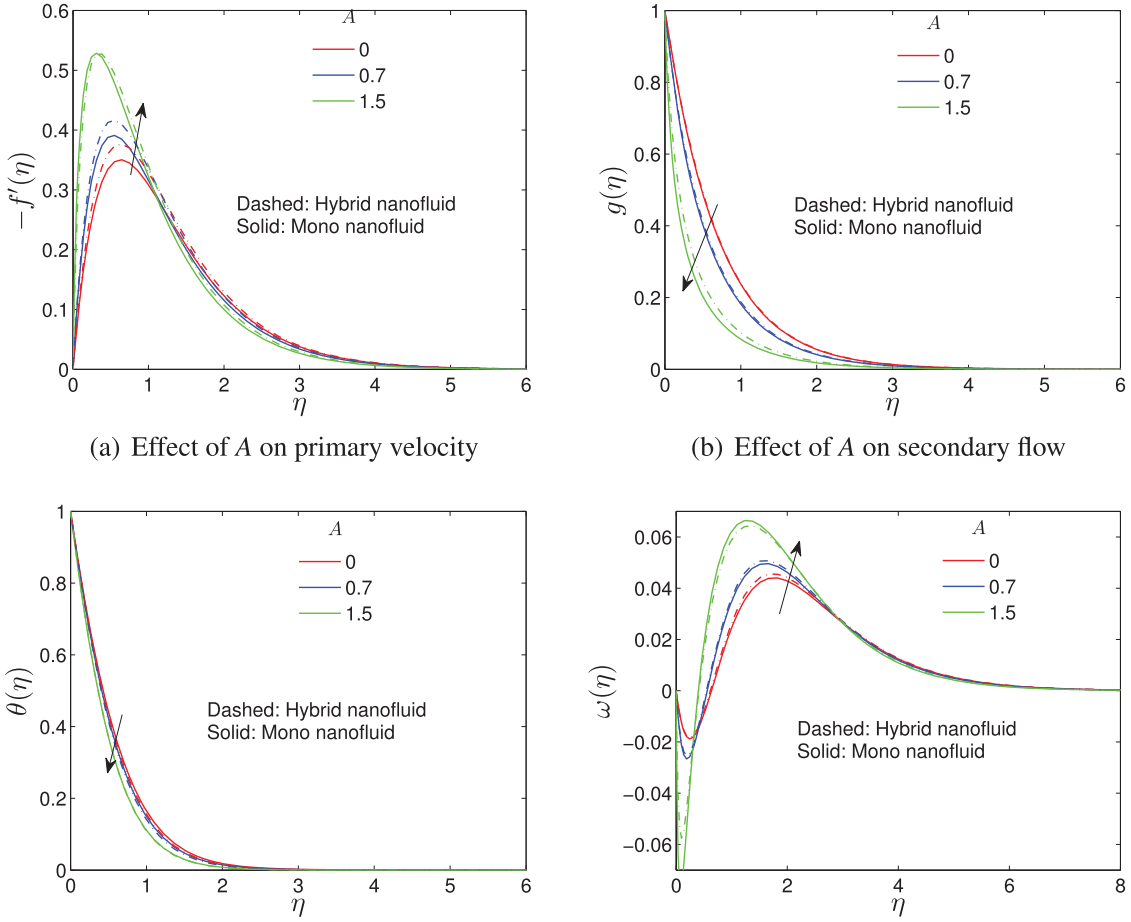

(a) Effect of A on primary velocity

(b) Effect of A on secondary flow

(c) Effect of A on temperatue

(d) Effect of A on microrotation

Figure 4: Variable viscosity parameter effect

In Tables 3 and 4, the flow behaviour for different values of radiation and magnetic parameter on local sikin friction effect and Nusselt number are presented. The cases for mono-nanofluids $Ag/water$, $MgO/water$ and hybrid nanofluid $Ag-MgO/water$ are studied. It is observed that both the local skin friction and the Nusselt number increases with an increase in the radiation and magnetic parameters.

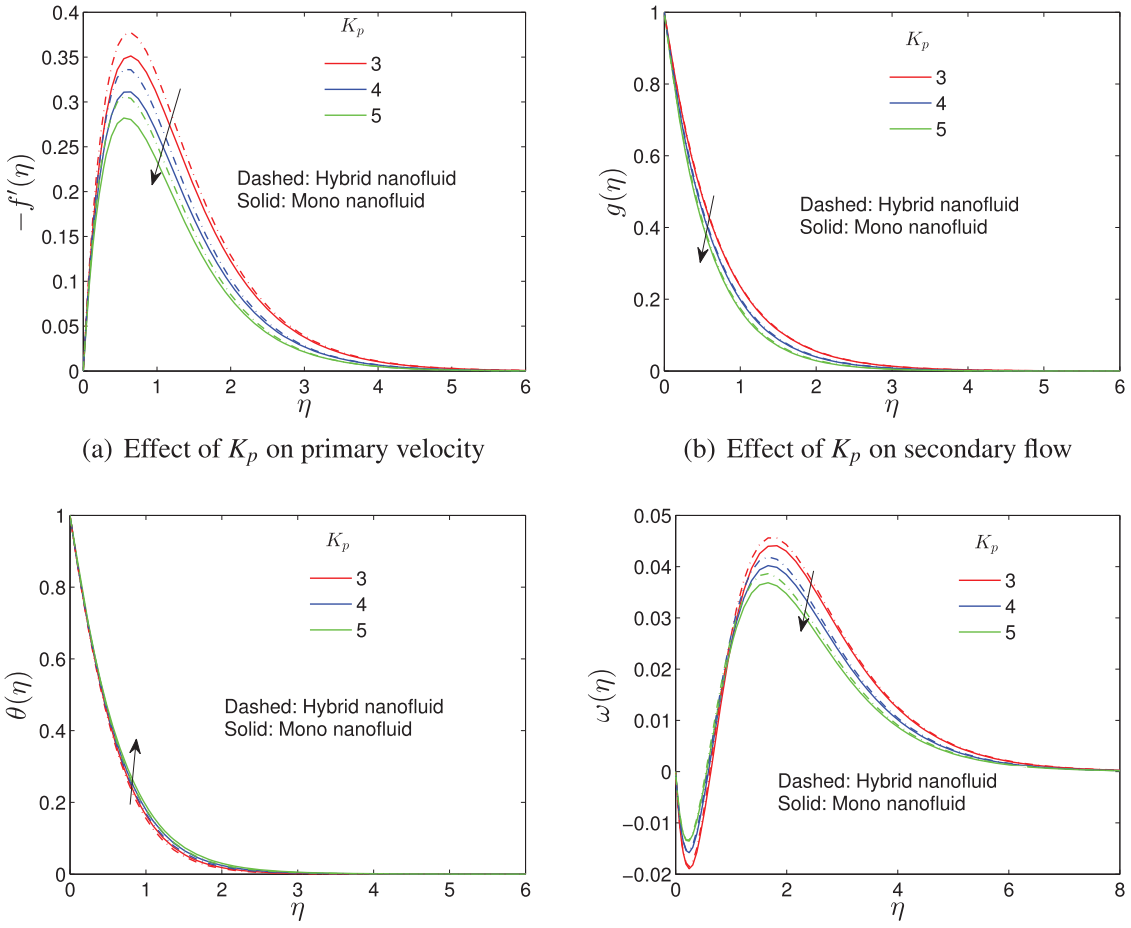

(a) Effect of K_p on primary velocity

(b) Effect of K_p on secondary flow

(c) Effect of K_p on temperatue

(d) Effect of K_p on microrotation

Figure 5: Porosity parameter effect

Table 3: Numerical values for the skin friction for radiation and magnetic parameter when $Pr = 6.8, \varepsilon = 0.2, s = 0.2, K_p = 3, B = 2, A = 0.02, K = 0.6, \lambda = 2$

Rd	M	$C_{fx}Re_x^{1/2}$ Ag/water $\phi_{Ag} = 0.018$	MgO/water $\phi_{MgO} = 0.02$	Ag-MgO/water $\phi_{Ag} = 0.018,\ \phi_{MgO} = 0.02$
0	0.5	1.50654604	1.39400943	1.51055932
0.5		1.58714921	1.46925102	1.59134563
1		1.64957488	1.52745004	1.65391613
2		1.74335788	1.61476788	1.74792167
0.7	0	1.58532802	1.45480453	1.58940010
	0.5	1.62023049	1.48181063	1.61808768

(Continued)

Table 3 (continued)

Rd	M	$C_{fx}Re_x^{1/2}$ Ag/water $\phi_{Ag} = 0.018$	MgO/water $\phi_{MgO} = 0.02$	Ag-MgO/water $\phi_{Ag} = 0.018,\ \phi_{MgO} = 0.02$
	0.7	1.62688155	1.49413268	1.63123346
	1	1.64843646	1.51443667	1.65295380

Table 4: Numerical values for local Nusselt number for radiation and magnetic parameter when $Pr = 6.8, \varepsilon = 0.2, s = 0.2, K_p = 3, B = 2, A = 0.02, K = 0.6, \lambda = 2$

Rd	M	$Nu_xRe_x^{-1/2}$ Ag/water $\phi_{Ag} = 0.018$	MgO/water $\phi_{MgO} = 0.02$	Ag-MgO/water $\phi_{Ag} = 0.018, \phi_{MgO} = 0.02$
0	0.5	1.59553867	1.59859185	1.59842638
0.5		2.17847585	2.16923979	2.18031405
1		2.68706423	2.66710340	2.68806367
2		3.56651381	3.52816566	3.56619957
0.7	0	2.37393855	2.35357564	2.37532767
	0.5	2.39255625	2.36863805	2.39063920
	0.7	2.39608230	2.37547258	2.39761170
	1	2.40746545	2.38668655	2.40907652

5 Conclusion

A numerical investigation for unsteady magneto micropolar $Ag-MgO$ hybrid nanofluid flow on an inverted rotating cone is considered. The analysis is conducted in the presence of thermal radiation and uniform magnetic field in a porous media. Using appropriate transformations, the system of partial differential equations that models the problem is converted to a system of ordinary differential equations. These equations are then solved numerically using the overlapping grid multidomain spectral quasilinearization method. The velocities, microrotation and temperature profiles are examined graphically for prominent parameters. The main results are presented below:

- Micropolar fluid assists the secondary flow and diminishes the main flow. The water hybrid nanofluid, $\phi_{Ag}+\phi_{MgO}$, enhances the main flow whereas it decreases the secondary flow compared to the mono-nanofluid ϕ_{MgO} water.
- The rotational effect for the hybrid nanofluid near the boundary is greater than that of the mono-nanofluid.
- For the water hybrid nanofluid, $\phi_{Ag} + \phi_{MgO}$, the variable viscosity parameter has a greater effect on velocity compared to the corresponding case of mono-nanofluid ϕ_{MgO} water.
- The variable viscosity parameter reduces the temperature for the hybrid nanofluid, $\phi_{Ag} + \phi_{MgO}$, compared to the mono-nanofluid ϕ_{MgO} water.

- The porosity parameter decreases the main flow; however, the inclusion of the hybrid nanofluid $\phi_{Ag} + \phi_{MgO}$ can enhance velocity.

Acknowledgement: The authors would like to thank the anonymous reviewers for their valuable comments.

Funding Statement: The authors received no specific funding for this study.

Author Contributions: The authors confirm contribution to the paper as follows: conceptualisation: Mekonnen S. Ayano; writing original draft: Mekonnen S. Ayano; methodology, code writing: Thokozani N. Khumalo, Stephen T. Sikwila; Matlab code creation and validation: Mekonnen S. Ayano, Thokozani N. Khumalo, Stephen T. Sikwila; analysis and interpretation of results: Mekonnen S. Ayano, Stanford Shateyi; final manuscript preparation: Mekonnen S. Ayano, Stephen T. Sikwila; validation of results: Mekonnen S. Ayano, Stanford Shateyi. All authors reviewed the results and approved the final version of the manuscript.

Availability of Data and Materials: The readers can contact the corresponding author and request the Matlab codes used to generate the data.

Conflicts of Interest: The authors declare that they have no conflicts of interest to report regarding the present study.

References

1. Delouei A, Atashafrooz M, Hasan S, Karimnejad S. The thermal effects of multi-walled carbon nanotube concentration on an ultrasonic vibrating finned tube heat exchanger. Int Comm Heat Mass Trans. 2022;135:106098.
2. Siavashi M, Miri J, Seyed M. Numerical performance analysis of a counter-flow double-pipe heat exchanger with using nanofluid and both sides partly filled with porous media. J Therm Anal Calorim. 2018;135(2):1595–610.
3. Izadi A, Siavashi M, Xiong Q. Impingement jet hydrogen, air and Cu-H_2O nanofluid cooling of a hot surface covered by porous media with non-uniform input jet velocity. Int J Hydrogen Energy. 2019;44(30): 15933–48.
4. Saleh H, Alali E, Ebaid A. Medical applications for the flow of carbon-nanotubes suspended nanofluids in the presence of convective condition using laplace transform. J Assoc Arab Univ Basic Appl Sci. 2017;24(1):206–12.
5. Wong KV, De Leon O. Applications of nanofluids: current and future. Adv Mech Eng. 2010;2:519659–70.
6. Mkhatshwa M, Motsa S, Ayano M, Sibanda P. MHD mixed convective nanofluid flow about a vertical slender cylinder using overlapping multi-domain spectral collocation approach. Case Stud Therm Eng. 2020;18:100598. doi:10.1016/j.csite.2020.100598.
7. Thameem BH, Sivaraj R, Subramanyam RA, Chamkha AJ. SWCNH/diamond-ethylene glycol nanofluid flow over a wedge, plate and stagnation point with induced magnetic field and nonlinear radiation-solar energy application. Eur Phys J Spec Top. 2019;228(12):2531–51. doi:10.1140/epjst/e2019-900048-x.
8. Akmal N, Sagheer M, Hussain S, Kamran A. Investigation of free convection in micropolar nanofluid with induced magnetic field. Eur Phys J Plus. 2019;134(5):179. doi:10.1140/epjp/i2019-12512-7.
9. Zeeshan A, Ellahi R, Hassan M. Magnetohydrodynamic flow of water/ethylene glycol based nanofluids with natural convection through a porous medium. Eur Phys J Plus. 2014;129(12):123. doi:10.1140/epjp/i2014-14261-5.

10. Hady FM, Ibrahim FS, Abdel-Gaied SM, Eid MR. Radiation effect on viscous flow of a nanofluid and heat transfer over a nonlinearly stretching sheet. Nanoscale Res Lett. 2012;7(1):26. doi:10.1186/1556-276X-7-229.
11. Liu L, Miao P, Xu Y, Tian Z, Zou Z, Li G. Study of PT/TiO_2 nanocomposite for cancer-cell treatment. J Photochem Photobiol B: Biol. 2010;98(3):207–10. doi:10.1016/j.jphotobiol.2010.01.005.
12. Noghrehabadi A, Behseresht A, Ghalambaz M, Behseresht J. Natural-convection flow of nanofluids over vertical cone embedded in Non-Darcy porous media. J Thermophys Heat Trans. 2013;27(2):334–41. doi:10.2514/1.T3965.
13. Sheikholeslami M, Gorji Bandpy M, Ellahi R, Hassan M, Soleimani S. Effects of mhd on cu-water nanofluid flow and heat transfer by means of CVFEM. J Magn Magn Mater. 2014;349(6):188–200. doi:10.1016/j.jmmm.2013.08.040.
14. Afify AA. The effect of radiation on free convective flow and mass transfer past a vertical isothermal cone surface with chemical reaction in the presence of a transverse magnetic field. Can J Phys. 2004;82(6):447–58. doi:10.1139/p04-009.
15. Makinde O, Aziz A. Boundary layer flow of a nanofluid past a stretching sheet with a convective boundary condition. Int J Therm Sci. 2011;50(7):1326–32. doi:10.1016/j.ijthermalsci.2011.02.019.
16. Mehmood Z, Mehmood R, Iqbal Z. Numerical investigation of micropolar casson fluid over a stretching sheet with internal heating. Commun Theor Phys. 2017;67(4):443. doi:10.1088/0253-6102/67/4/443.
17. El-Kabeir SMM, Abdou MM. Chemical reaction, heat and mass transfer on MHD flow over a vertical isothermal cone surface in micropolar fluids with heat generation/absorption. Appl Math Sci. 2007;1: 1663–74.
18. Parveen K, Banse V, Ledwani L, Green synthesis of nanoparticles: Their advantages and disadvantages. AIP Conf Proc. 2016;1724:020048. doi:10.1063/1.4945168.
19. Chahregh HS, Dinarvand S. TiO_2-Ag/blood hybrid nanofluid flow through an artery with applications of drug delivery and blood circulation in the respiratory system. Int J Numer Methods Heat Fluid Flow. 2020;30(11):4775–96. doi:10.1108/HFF-10-2019-0732.
20. Ali K, Ahmad S, Ahmad S, Tayebi T. Impact of magnetic field localization on the vortex generation in hybrid nanofluid flow. J Thermal Anal Calorim. 2023;148(13):6283–300. doi:10.1007/s10973-023-12104-5.
21. Bhatti MM, Abbas T, Rashidi M. Effects of thermal radiation and electromagnetohydrodynamics on viscous nanofluid through a riga plate. Multidiscip Model Mater Struct. 2016;12(4):605–18. doi:10.1108/MMMS-07-2016-0029.
22. Liu Y, Jian Y, Tan W. Entropy generation of electromagnetohydrodynamic (EMHD) flow in a curved rectangular microchannel. Int J Heat Mass Trans. 2018;127:901–13. doi:10.1016/j.ijheatmasstransfer.2018.06.147.
23. Bilal M, Mazhar SZ, Ramzan M, Mehmood Y. Time-dependent hydromagnetic stagnation point flow of a Maxwell nanofluid with melting heat effect and amended Fourier and Fick's laws. Heat Trans. 2021;50(5):4417–34. doi:10.1002/htj.22081.
24. Ghadikolaei S, Hosseinzadeh K, Ganji D. Numerical study on magnetohydrodynic CNTS-water nanofluids as a micropolar dusty fluid influenced by non-linear thermal radiation and joule heating effect. Powder Technol. 2018;340:389–99. doi:10.1016/j.powtec.2018.09.023.
25. Sandeep N, Samrat SP, Ashwinkumar GP. Flow and heat transfer in radiative MHD dusty-hybrid ferrofluids. Waves Random Complex Media. 2022;66:1–14. doi:10.1080/17455030.2022.2036866.
26. Nazar R, Amin N, Grosan T, Pop I. Free convection boundary layer on a sphere with constant surface heat flux in a micropolar fluid. Int Commun Heat Mass Trans. 2002;29(8):1129–38. doi:10.1016/S0735-1933(02)00441-4.
27. Braga VM, Barbosa JR, Deschamps C. Numerical investigation of refrigerant outgassing in the screw pump of a hermetic reciprocating compressor oil supply system. Proc Inst Mech Eng, Part E: J Process Mech Eng. 2020;236(1):87–93. doi:10.1177/0954408920952609.

28. Rehman F, Khan MI, Sadiq M, Malook A. MHD flow of carbon in micropolar nanofluid with convective heat transfer in the rotating frame. J Mol Liq. 2017;231:353–63. doi:10.1016/j.molliq.2017.02.022.
29. Malik M, Jamil H, Salahuddin T, Bilal S, Rehman K, Mustafa Z. Mixed convection dissipative viscous fluid flow over a rotating cone by way of variable viscosity and thermal conductivity. Results Phys. 2016;6(7):1126–35. doi:10.1016/j.rinp.2016.11.027.
30. Ahmad S, Ali K, Bashir H. Interaction of micropolar fluid structure with the porous media in the flow due to a rotating cone. Alex Eng J. 2021;60(1):1249–57. doi:10.1016/j.aej.2020.10.048.
31. Ayano M, Motsa S, Otegbeye O. A paired quasilinearization method for solving the MHD mixed convection flow of a micropolar fluid through a truncated cone in a non-darcy porous medium. Theor Appl Mech. 2019;46(2):173–89. doi:10.2298/TAM190801011S.
32. Hiba B, Redouane F, Jamshed W, Ahamed SC, Suriya UDS, Prakash M, et al. A novel case study of thermal and streamline analysis in a grooved enclosure filled with (Ag-MgO/Water) hybrid nanofluid: galerkin FEM. Case Stud Therm Eng. 2021;28:101372.
33. Khan MI, Alzahrani F. Free convection and radiation effects in nanofluid (silicon dioxide and molybdenum disulfide) with second order velocity slip, entropy generation, Darcy-Forchheimer porous medium. Int J Hydrogen Energy. 2021;46(1):1362–9.
34. Mkhatswa MP. Overlapping grid spectral collocation methods for nonlinear differential equations modelling fluid flow problems (Ph.D. dissertation). University of KwaZulu-Natal: South Africa; 2020.
35. Motsa SS, Sibanda P, Shateyi S. On a new quasi-linearization method for systems of nonlinear boundary value problems. Math Methods Appl Sci. 2011;34(11):1406–13.
36. Chamkha AJ, Al-Mudhaf A. Unsteady heat and mass transfer from a rotating vertical cone with a magnetic field and heat generation or absorption effects. Int J Therm Sci. 2005;44(3):267–76.